Published in final edited form as:
J Control Release. 2010 June 15; 144(3): 288–295. doi:10.1016/j.jconrel.2010.02.030.

Ultrasound-enhanced delivery of targeted echogenic liposomes in a novel *ex vivo* mouse aorta model

Kathryn E. Hitchcock[*], **Danielle N. Caudell**[§], **Jonathan T. Sutton**[*], **Melvin E. Klegerman**[#], **Deborah Vela**[Δ], **Gail J. Pyne-Geithman**[§], **Todd Abruzzo**[‡], **Peppar E. P. Cyr**[*], **Yong-Jian Geng**[#], **David D. McPherson**[#], and **Christy K. Holland**[*]

[*]Department of Biomedical Engineering, University of Cincinnati, Cincinnati, OH

[§]Department of Neurology, University of Cincinnati, Cincinnati, OH

[#]Department of Internal Medicine, University of Texas Health Science Center, Houston, TX

[Δ]Texas Heart Institute

[‡]Departments of Neurosurgery and Radiology, Cincinnati Children's Hospital Medical Center

Abstract

The goal of this study was to determine whether targeted, Rhodamine-labeled echogenic liposomes (Rh-ELIP) containing nanobubbles could be delivered to the arterial wall, and whether 1 MHz continuous wave ultrasound would enhance this delivery profile. Aortae excised from apolipoprotein-E-deficient (n = 8) and wild-type (n = 8) mice were mounted in a pulsatile flow system through which Rh-ELIP were delivered in a stream of bovine serum albumin. Half the aortae from each group were treated with 1-MHz continuous wave ultrasound at 0.49 MPa peak-to-peak pressure, and half underwent sham exposure. Ultrasound parameters were chosen to promote stable cavitation and avoid inertial cavitation. A broadband hydrophone was used to monitor cavitation activity. After treatment, aortic sections were prepared for histology and analyzed by an individual blinded to treatment conditions. Delivery of Rh-ELIP to the vascular endothelium was observed, and subendothelial penetration of Rh-ELIP was present in five of five ultrasound-treated aortae and was absent in those not exposed to ultrasound. However, the degree of penetration in the ultrasound-exposed aortae was variable. There was no evidence of ultrasound-mediated tissue damage in any specimen. Ultrasound-enhanced delivery within the arterial wall was demonstrated in this novel model, which allows quantitative evaluation of therapeutic delivery.

Keywords

ultrasound-assisted delivery; liposomes; ICAM-1 targeting; vascular endothelium; atheroma

Corresponding Author: Kathryn E. Hitchcock, MSB 6152, 231 Bethesda Ave., Cincinnati, OH 45267-0586, 513-558-5505, Fax: 513-558-6102, hitchcke@email.uc.edu.

Introduction

Providing efficient and safe methods for the delivery of drugs to target cells is the principal goal of a clinically useful pharmacotherapeutic strategy. When a drug is administered systemically only a small fraction of the drug may actually reach the target tissue, with the necessity of large total doses to achieve effective local concentrations. Hence, systemic toxicity is usually the dose-limiting factor [1]. Direct delivery of a drug to the target organ results in a high ratio of local to systemic bioavailability, with the result that total required dose is decreased [2]. As a result, targeted delivery may result in increased tolerable concentrations of the drug.

For atherosclerosis, an ideal targeted delivery agent could deliver large payloads of therapeutics to the active atheroma, stabilizing the area prone to rupture while minimizing systemic and nonspecific drug effects. This would be a tool of critical importance for physicians in cases of known carotid or coronary artery disease when direct, definitive treatment could obviate the need for risky surgery.

Liposomes are ideal targeted delivery systems as they are relatively nontoxic and can carry hydrophilic or hydrophobic compounds either in the aqueous compartment or within the phospholipid bilayers, respectively. Liposomes may be targeted to a particular tissue by incorporating antibodies for a desired antigen into their outer membranes [3], [4], [5]. We have developed an echogenic targeted liposomal complex that can incorporate drugs and deliver them directly to cells [6], [7], [8], [9]. In atherosclerosis, intercellular adhesion molecule 1 (ICAM-1) has been observed to be upregulated on the cell surfaces of the endothelium overlying atheromatous plaques making it one possible target to select for the liposomal complex [10], [11], [12].

Acoustic cavitation has been studied extensively both theoretically and experimentally by investigators in an attempt to understand the cause of ultrasound bioeffects [13], [14], [15], [16], [17], [18], [19], [20], [21], [22], [23], [24], [25]. Acoustic cavitation is the formation and collapse of vapor bubbles in a liquid due to an acoustic pressure field. Cavitation is generally classified into two types: stable cavitation, which results in emissions at subharmonics of the main excitation frequency, and inertial cavitation, which is characterized by broadband noise emissions. When a bubble oscillates nonlinearly about its equilibrium radius, Faraday waves are excited along the bubble wall, causing subharmonic emissions [26]. Broadband noise emissions are generated when bubbles undergo large radial oscillations and collapse violently [19], [24], [27]. This latter type of bubble motion is dominated by the inertia of the surrounding fluid, hence the label “inertial” cavitation.

Enhanced penetration of a thrombolytic has been demonstrated in *in vitro* porcine clot model [28]. Significant enhancement of thrombolysis correlates with the presence of stable cavitation [29] and this type of gentle bubble activity can be sustained using an intermittent infusion of a commercial contrast agent, Definity®. We aim to harness the potential of stable cavitation nucleated by echogenic liposomes for therapeutic benefit, with the specific goal of enhancing the penetration of therapeutics across the arterial wall to treat atheromata.

In our previous work, liposomes have been used to entrap micro- and nanobubbles, enabling enhanced echogenicity and cavitation nucleation [30]. The use of ultrasound to fragment drug-loaded echogenic liposomes (ELIP) near the target tissue, rather than relying on more gradual passive release, has the potential to produce a large temporal peak in drug or therapeutic effect. This is particularly important at the endothelium where the constant flow of blood may carry away the released drug rapidly, making it unavailable for uptake across the endothelium.

This study uses a novel *ex vivo* murine arterial model to examine delivery of Rhodamine-labeled and anti-ICAM-1-targeted echogenic liposomes (Rh-ELIP) to, and possibly beyond, the endothelium. We tested the hypothesis that low-intensity continuous wave (CW) ultrasound (0.49 MPa peak-to-peak pressure amplitude) enhances Rh-ELIP delivery in an *ex vivo* mouse aorta with flow. Specifically, 1-MHz CW ultrasound will increase the transport of Rh-ELIP across the endothelium by nucleating stable cavitation. Our *ex vivo* test model used murine wild-type and atheromatous aortae and allowed quantification of Rh-ELIP in the intravascular and perivascular fluids separately. This platform provides a model system for evaluation of delivery methodologies to the arterial wall.

Materials and Methods

Excised mouse aortae were mounted in a flow system, infused with Rh-ELIP in the intraluminal fluid, and exposed to 1-MHz CW ultrasound while cavitation was detected acoustically. The mouse aorta was chosen to take advantage of an existing model of atherosclerosis, as there is interest in using a combination of ELIP and ultrasound to deliver drugs into atheromata in order to arrest their development. An *ex vivo* technique was chosen in order to allow precise control of flow parameters. This approach also permitted careful observation of the effects of ultrasound on the intra-arterial fluid in the presence of an intact, viable endothelium.

Formulation of Rhodamine-labeled ELIP

Rhodamine-labeled ELIP were prepared by the dehydration-lyophilization-rehydration method as described previously [31]. The ELIP composition used was a combination of lipids, egg PC: MPBPE: DPPG:CH in a 69:8:8:15 molar ratio, where PC is phosphatidylcholine; MPB-PE is 1,2-dipalmitoylsn-glycero-3-phosphoethanolamine-N-[4-(p-maleimidophenyl) butyrate], DPPG is dipalmitoylphosphatidylglycerol, and CH is cholesterol. Rhodamine B-PE (Avanti Polar Lipids, Alabaster, AL, USA), 0.25 mole%, was included in the formulation, which was subsequently protected from exposure to light. The component lipids were dissolved in chloroform and the solvent was allowed to evaporate completely. The resulting lipid film was placed under vacuum for full drying and then rehydrated with distilled, deionized water. This dispersion was sonicated until a desired mean size (500 nm) was obtained, based on the relationship of a turbidity measurement to the average liposome size using optical absorbance at 440 nm [32]. An equal volume of 0.2 M D-Mannitol was added to the liposome suspension and the sample was frozen at −70° C. The samples were lyophilized for 48 hours and stored at 4 °C.

For conjugation, 0.4 mg monoclonal anti-human/mouse ICAM-1 (Santa Cruz Biotechnology, Santa Cruz, CA, USA), and 1.6 mg nonspecific mouse immunoglobulin G(IgG) were reacted with 3-(2-pyridyldithiolpropionic acid)-N-hydroxysuccinimide ester (SPDP) at a SPDP:IgG protein molar ratio of 15:1 for 30 min at 24 ± 1 °C. Protein was separated from unreacted SPDP by gel chromatography on a 50 ml Sephadex G-50 column (Sigma-Aldrich, St. Louis, MO, USA) equilibrated with 0.05M citrate-phosphate buffer at a pH of 5.5. Protein fractions were identified using a spectrophotometric technique (Genesys 10uv, Thermo Electron Corp., Milford, MA) at a wavelength of 280 nm, pooled and concentrated to ≤ 2 ml using Centricon YM-10 centrifugal filter units (Millipore, Billerica, MA, USA). The SPDP-activated protein was reduced in 25mM dithiothreitol (DTT) for 30 min at 24 ± 1 °C. The thiolated protein was isolated using a Sephadex G-50 column, equilibrated and eluted with pH 6.7 citrate-phosphate buffer.

The thiolated protein was reacted with reconstituted Rh-ELIP (10mg lipid/ml 0.1 M phosphate buffer at a pH of 6.62) under argon overnight at 24 ± 1 °C. Rh-ELIP were separated from free protein and low molecular weight products by gel filtration on a 20-ml Sepharose CL-4B column (Sigma-Aldrich) that had been pre-saturated with unconjugated, unlabeled ELIP

according to the method of Lasch et al. [33] and [9] and eluted with 0.02 M phosphate-buffered saline (PBS) at a pH of 7.4. Liposome-containing fractions were identified by optical absorbance at a wavelength of 440 nm prior to elution of free IgG. The Rh-ELIP were lyophilized with 0.1M D-mannitol. The size distribution of these liposomes, as assessed by dynamic light scattering and quantitative acoustic backscattering measurements, is complex and heterogeneous [34]. The majority of ELIP (95% by number density) have a mean diameter of 100 nm. However some have a mean diameter of 1.0 μm (4.5%) and a few others have an even larger mean diameter of 4.5 μm (0.5%) [34].

To verify their physical properties, ELIP (5 mg lipid) were freshly reconstituted and diluted in water to a concentration of 1.0 mg lipid/ml, then subjected to a negative staining procedure with 1% uranyl acetate on 300 mesh formvar carbon grids (EMS, Hatfield, PA, USA). Stained samples were examined with a JEOL 1200 transmission electron microscope (Tokyo, Japan) at 60 kV. Images were captured using a Gatan BioScan 792 CCD camera (Pleasanton, CA, USA).

Ex vivo flow system

Male (n=8), 24-week-old mice from the strain C57BL/6J were obtained from Jackson Laboratories (Bar Harbor, ME, USA). Male (n=5) and female (n=3) 17-week old, homozygous, apoE knockout (apoE −/−) mice of C57BL/6J background were obtained from the Center for Laboratory Animal Medicine and Care at the University of Texas Houston, which had been bred there from a strain purchased from Jackson laboratories. Animals were sacrificed using gaseous carbon dioxide in accordance with a protocol approved by the University of Cincinnati Institutional Animal Care and Use Committee. Mice were perfused with room temperature saline (0.9%) via cannulation of the left ventricle until blood was no longer visible in the perfusate. Aortae were excised within 5 minutes of perfusion and dissected free of connective tissue in ice-cold saline. The collateral arteries including the visceral and parietal branches of the aorta and the celiac arteries were heat cauterized.

The prepared artery was mounted on cannulae made from blunted 25-gauge hypodermic needles, and fixed within a stainless steel and Delrin® frame. An acoustically transparent latex wall was expanded around the chamber, and the volume around the artery was filled with normal saline to keep the artery wet, provide acoustic coupling, and contain any Rh-ELIP that emerged from the artery. Shown in Figure 1, panel A, is an *ex vivo* artery mounted in the sample chamber.

The excised artery within its chamber was connected via the cannulae to a flow system consisting of a reciprocating pump designed to mimic rodent circulation, an oxygen-filled gas exchanger, a preload chamber, an afterload chamber, and a fluid reservoir. Through the system and artery, 0.5% BSA in phosphate buffered saline (Sigma Aldrich, St. Louis, MO, USA) was circulated at a flow rate of 3.4 mL/min with a stroke rate of 200 beats per minute. Some of the flow was diverted through a bypass around the artery in order to control the pressure to which the vessel was exposed, such that the flow rate through the artery itself was 2.6 mL/min. This flow rate is within the physiologic range of blood flow in the murine aorta (1.4 – 7.7 ml/min) and minimizes leaks from the artery[35].

Using an inline catheter, 1.5 mL of Rh-ELIP in 0.5% BSA were injected proximal to each artery with a catheter concentration of 3.33 mg lipid/mL and a catheter flow rate of 3 mL/min. The flow rate in the aorta during a 30-second ELIP bolus injection was 5.2 mL/min. Thus, the diluted arterial concentration of ELIP was 1.8 mg lipid/mL (approximately 8.1×10^9 liposomes/mL). This liposomal concentration has been shown to be well tolerated in a Yucatan miniswine atherosclerosis model [36], [37]. For two additional arteries from apoE knockout mice (one with ultrasound exposure, one without), the bolus of Rh-ELIP was injected directly into the

perivascular fluid in order to assess the histological effect of maximum Rh-ELIP leakage on the arterial tissue.

Ultrasound delivery and cavitation detection

The *ex vivo* artery mounted in the sample chamber (shown in Figure 1, panel A) was suspended in a tank filled with 37 °C purified and degassed water (shown in Figure 2). The artery was aligned at the Rayleigh distance of a 2.5-cm, 1-MHz single element unfocused ultrasound transducer (Panametrics, Waltham, MA, USA) with a 10 mm 3-dB beam width and 6.0-cm depth of field. A prototype, broadband cylindrically focused hydrophone designed for passive cavitation detection [19] (Sonic Concepts Inc., Woodinville, WA, USA) was aligned 90° to the beam of the 1-MHz transducer so that the confocal region encompassed the artery. The water tank was lined with acoustically absorbent rubber to prevent acoustic reflections and the formation of standing waves.

The stable and inertial cavitation thresholds for ELIP suspended in BSA flowing inside an *ex vivo* mouse aorta were measured. These thresholds were used to select an ultrasound pressure amplitude for the exposure of *ex vivo* mouse aortae to be treated with Rh-ELIP. A passive cavitation detection technique [29], [38] was used to determine the stable and inertial cavitation thresholds during insonation with 1-MHz CW ultrasound.

The transducer and hydrophone were aligned to each artery, regardless of the ultrasound exposure condition. For those arteries that received ultrasound treatment, the transducer cable was connected to the amplifier when the Rh-ELIP bolus was visually confirmed to be exiting from the artery, and was left connected for 30 seconds [39], [40]. The artery was insonified with 1-MHz CW ultrasound at a peak-to-peak pressure of 0.49 MPa and the passive cavitation detector was used to verify the duration of the resulting stable cavitation. This sound pressure level was chosen to be above the threshold of stable cavitation and below the threshold of inertial cavitation in 0.5% BSA with ELIP flowing through a mouse aorta as measured by the prior experiments. After the arteries were exposed or sham exposed to ultrasound, flow of 0.5% BSA was allowed to continue through the artery for three minutes following the passage of the Rh-ELIP to provide a wash. The artery was removed, marked with India ink (Koh-I-Noor, Bloomsbury, NJ, USA) for orientation, sliced in cross section, snap-frozen in Tissue-Tek Optimal Cutting Temperature compound (Sakura Finetek, Torrance, CA, USA), and stored at −80°C. The perivascular saline was collected and analyzed in a spectrofluorometer (Shimadzu, Kyoto, Japan) for the presence of Rh-ELIP.

Fluorometric quantification of Rh-ELIP in perivascular fluid

Fluorescence and absorbance spectra from solutions of reconstituted Rh-ELIP in normal saline over a range of concentrations were gathered using an RF-5301 PC spectrofluorophotometer and a UV-1700 spectrophotometer (Shimadzu Corporation, Kyoto, Japan), respectively. An excitation wavelength of 567 nm was used for all spectrofluorometric measurements because it coincided with the maximum absorbance for Rh-ELIP. Similarly, fluorescence spectra were acquired from solutions of BSA over a range of concentrations (0 to 0.5%). Fluorescence peaks from measurement of the perivascular fluid were noted at 589 nm due to the presence of Rh-ELIP and at 675 nm due to the presence of BSA. However, a tail of the BSA peak overlapped with the Rh-ELIP peak at 589 nm. Therefore to determine the concentration of Rh-ELIP in the perivascular fluid after intravascular injection and ultrasound or sham ultrasound treatment, the fluorescence intensity at 589 nm was corrected for the contribution of fluorescence due to BSA.

The collected perivascular fluid was refrigerated in a sealed, covered container protected from light following each experimental treatment. Prior to fluorometric measurement, the fluid was

allowed to equilibrate to 22 ± 1 °C. The volume was measured with a graduated cylinder and a fluorescence spectrum gathered. Because the total volume of perivascular fluid changed from one sample to the next, each measured concentration was normalized by multiplying by the total volume. This normalized concentration (in units of mass) could be compared between trials. To assess this assay's integrity over time, Rh-ELIP fluorescence intensity was monitored as a function of time after Rh-ELIP reconstitution. A solution of Rh-ELIP at 25 μg/mL did not show a significant deviation in fluorescence intensity over the course of 24 hours (< ± 7 arbitrary units) when protected from light. Therefore, all fluorescence measurements of perivascular fluid were taken within this time window.

The ability to measure Rh-ELIP accurately at low concentrations was limited by the amount of BSA present in the perivascular fluid. To assess the lowest Rh-ELIP concentration sensitive to detection, the *ex vivo* model was injected with Rh-ELIP in the absence of a mounted artery, allowing the entire bolus to accumulate in the perivascular fluid. The fluorescence spectrum was gathered to determine the lowest Rh-ELIP concentration detectable. The Rh-ELIP concentration detected in the perivascular fluid also served as a positive control, demonstrating what portion of the 5 mg of lipid injected entered the artery chamber in the presence of a complete leak.

Tissue histology

Each arterial segment was cut on a cryostat into five-micron-thick sections and mounted on glass slides. One section was stained with hematoxylin and eosin for routine histologic evaluation. An additional section was immunostained for the endothelial cell marker Factor VIII-related antigen (Dako North America, Carpinteria, CA, USA) to highlight the intimal layer of the specimens. Another section was immunostained with rat antibody against mouse ICAM-1 (Stemcell Technologies, Vancouver, BC, Canada) in order to locate regions of ICAM-1 expression on the endothelium. Unstained sections were examined under fluorescence microscopy with an Olympus BX61 microscope equipped with a Retiga 2000R FAST 1394 FireWire monochrome 12 bit cooled digital camera (Olympus America, Center Valley, PA, USA), to determine the adherence or penetration of Rh-ELIP into the arterial wall. Image analysis was processed with Olympus Microsuite™ Biological Suite software (v. 5.0, Olympus America) on a Dell Optiplex GX270 computer (Dell, Round Rock, TX, USA).After histological preparation, a representative set of slides was assessed by an individual blinded to the ultrasound exposure conditions. For each arterial section, a photomicrograph was rendered with light microscopy, with a red fluorescent filter alone, and with the red-filtered image superimposed on a blue-filtered image to demonstrate the elastic lamellae of the arterial wall as shown in Figure 3. The endothelium was examined for the presence of red fluorescence beyond the background red autofluorescence of the arterial tissue. Additionally, a routine was written in MATLAB (Mathworks Inc., Natick, MA) that allowed a blinded assessor to quantify the amount of Rh-ELIP present in the subendothelial tissues by selecting an appropriate redness threshold, summing the red pixels (with each weighted by its intensity), and using a scale in the image to convert from pixel area to μm^2. This red area was then normalized by the inner perimeter of the artery to account for variations in artery size. The Wilcoxon–Mann– Whitney test was applied to the quantified Rh-ELIP penetration data using GraphPad's StatMate Software (GraphPad Software, Inc, San Diego, CA).

Results

Electron microscopy of ELIP

Liposomes in the transmission electron micrographs produced at 150,000X magnification were very heterogeneous in appearance and size, ranging from about 45 to 400 nm in diameter. This is consistent with prior particle size analyses, in which the number average distribution

indicated that particles < 400 nm were in great preponderance relative to larger particles. Lipid bilayers could be seen clearly surrounding numerous liposomes in all the figures. The width of the bilayers varied from 5 to about 11 nm, suggesting distention of some bilayers, perhaps by small gas nanobubbles. Most striking are numerous electron transparent spheres in the lumen of more electron dense vesicles (Figure 4), corresponding to areas of gas localization as discussed by Kodama et al. [41]. In some cases, the gaseous spheres appear to be surrounded by a distinct monolayer (black arrows) within the lumen of the liposome, while in others, there is no discernable boundary between the electron transparent regions and the surrounding intravesicular fluid. The gas in the vesicular lumen is likely stabilized by surface tension.

Cavitation thresholds

With non-ICAM-1-targeted ELIP delivered during steady flow at a concentration of 1.8 mg/mL of lipid through the artery, the stable cavitation threshold during insonation with 1-MHz CW ultrasound was 0.43 ± 0.02 MPa peak-to-peak pressure amplitude, and the inertial cavitation threshold was 0.51 ± 0.01 MPa. Based on these results, 1-MHz CW ultrasound can be applied to *ex vivo* arteries with ELIP to achieve stable cavitation or inertial cavitation at low peak-to-peak acoustic pressure amplitudes.

When arteries were exposed to a 0.49 MPa peak-to-peak pressure amplitude, passive cavitation signals from arteries treated with both Rh-ELIP and 1-MHz ultrasound displayed strong peaks at one half of the fundamental frequency as well as odd multiples of this subharmonic. No increase in broadband signal was present. This indicates that the arteries were exposed to stable cavitation, but not inertial cavitation. The stable cavitation signal persisted throughout the 30-second treatment period for each artery exposed to ultrasound.

Spectrofluorometric assessment of Rh-ELIP Concentration

Shown in Figure 5 is the fluorescence intensity for Rh-ELIP in normal saline as a function of Rh-ELIP concentration (0–50 μg lipid/mL saline). Data points represent the mean of three measurements and error bars represent the standard deviation. The largest tail of the BSA fluorescence intensity at 589 nm for a positive control (no artery present) was 14.8 arbitrary units (AU). The Rh-ELIP concentration measured in this positive control was 59.8 μg/mL, corresponding to 84.7 AU. The lowest Rh-ELIP concentration detectable, 2.44 μg/mL (or 0.19 mg), was determined by adding two standard deviations above the mean BSA emission intensity. The concentration of Rh-ELIP in the perivascular saline was identical in arteries that were exposed or sham exposed to ultrasound. As shown in Figure 6, the normalized concentration (or mass) of Rh-ELIP that leaked into the perivascular fluid was the same for all arteries, and was less than the mass present in a positive control.

Rh-ELIP fluorescence histology

Enhanced fluorescence was observed on the endothelial cells of mouse aortae exposed to anti-ICAM-targeted as shown in Figure 3, panels B and C. As this fluorescence was qualitatively greater than the autofluorescence of arteries not exposed to Rh-ELIP, the endothelial enhancement was interpreted as successful targeting of Rh-ELIP to the endothelium. This enhancement was observed in six of seven arteries exposed to 1-MHz ultrasound, and in five of seven arteries not exposed to ultrasound. In some arteries, penetration beyond the endothelium was observed as shown in Figure 3, panel C. The diseased arteries (from apoE knockout mice) did not exhibit a greater adherence of Rh-ELIP on the endothelium overlying the atheromatous plaques. Both arteries for which the 5 mg of Rh-ELIP was intentionally added to the perivascular fluid instead of injected into the lumen showed no enhanced red fluorescence across the arterial wall.

Analysis of Rh-ELIP targeting and ultrasound treatment

In 10 of 10 arteries exposed to intravascular Rh-ELIP in flowing BSA, Rhodamine-enhanced red-filtered fluorescence was observed on the endothelium. As demonstrated in Figure 7, sites of Rh-ELIP location corresponded well with sites of ICAM-1 expression on the endothelium. There were 16 arteries originally in the treatment groups, but two yielded histology deemed unreadable by the assessor blinded to experimental conditions. Additionally, analysis of slides produced by immunostaining with the endothelial cell marker Factor VIII-related antigen showed that four arteries had endothelia that were entirely absent. This occurred in two arteries that were exposed to ultrasound and two that were not, and was likely due to excessive handling while placing the arteries into the flow system. In prepared slides of the remaining arteries the endothelium appeared either intact or partially desquamated, with desquamated cells present in the arterial lumen. This desquamation was observed in both treated and control segments and was determined to be an artifact of tissue embedding by a pathologist also blinded to experimental conditions.

It was hypothesized that ultrasound exposure of arteries during the Rh-ELIP bolus would result in enhanced penetration of the liposomes beyond the endothelial layer. In five of five arteries treated with ultrasound, penetration beyond the endothelium was observed, whereas none of the five arteries without ultrasound displayed sub-endothelial penetration. Shown in Figure 8 are the results of a quantitative assessment of the penetration of Rh-ELIP into the sub-endothelial tissues via image analysis of the histological slides of the aortae.

A one-tailed Wilcoxon–Mann–Whitney test showed that penetration of Rh-ELIP past the aortic endothelium is significantly greater in US-exposed arteries, with a p-value of 0.02. Rh-ELIP were never observed throughout the entire thickness of the arterial wall. The deepest red fluorescence was observed in an ultrasound-treated aorta at the fourth of six visible elastic lamellae in the tunica media, numbering from lumen to adventitia.

Arterial bioeffects

Handling of the arteries resulted in the loss of the delicate endothelial tissue in four of sixteen arteries, two that were subsequently treated with ultrasound and two that were not. In the remaining specimens, blinded pathologic assessment of each mouse aorta following treatment, mounting, and staining revealed no signs of cellular or structural damage in any of the arteries, with or without ultrasound exposure. The slight separation between the smooth muscle cells and the elastic lamellae that appeared in some portions of the artery, in both treated and control segments, was determined to be an artifact of tissue processing (Figure 3).

Discussion

The strength of the *ex vivo* model described here lies in the ability to quantify the delivery of fluorescently labeled liposomes to the lumen separately from the adventitia and beyond in an intact, living artery. Note that the isolated, perfused artery system allows separation of the luminal perfusate from the perivascular fluid. In addition, tight control of flow parameters and careful detection of the bubble dynamics help to reveal the mechanism mediating the penetration of Rh-ELIP. This model provides pulsatile flow that mimics blood flow dynamics and endothelial shear stress similar to that observed in whole animal models [35]. Quantification of luminal versus extravascular delivery of molecules can be correlated with the presence of ultrasound-induced bubble activity in this platform.

Similar to previous reports in a porcine model *in vivo* [36], anti-ICAM-1-conjugated ELIP targeted and adhered to the vascular endothelium. Like the porcine *in vivo* study by Demos et al. [36], intraluminal flow did not prevent adherence of Rh-ELIP to the vascular endothelium

in our *ex vivo* model. Passage of Rh-ELIP beyond the endothelium was confirmed by histology, and verified the enhanced echogenicity within the dense adventitia observed by Hamilton et al. [37] with intravascular ultrasound. Successful targeting has also been observed *in vitro* by Bloemen et al. [42] who demonstrated localization of anti-ICAM-targeted RhELIP to cultured human umbilical vein endothelial cells.

The effect of 1-MHz ultrasound exposure on the transendothelial delivery of Rh-ELIP was explored in this study. Ultrasound exposure produced a greater incidence of Rh-ELIP penetration beyond the endothelial layer. In arteries with immature atheromata in which drug delivery into the tunica media could be of great clinical importance, this outcome points to a potentially useful technique. This is especially true when taken in light of previous studies, in which essentially immediate phagocytosis of liposomes by the endothelial cells was observed [43].

Previous studies have shown ultrasound-mediated extravasation of red blood cells in the presence of gas-filled ultrasound contrast agents. However, penetration of Rh-ELIP beyond the third elastic lamina of the tunica media was not observed in our study. Arteries exposed to ultrasound showed similar quantities of Rh-ELIP in the perivascular saline to those arteries with no ultrasound treatment. Additionally, those arteries with Rh-ELIP intentionally injected into the extravascular fluid (positive controls) did not exhibit arterial wall penetration of Rh-ELIP on histology. Therefore we conclude that the high concentrations of Rh-ELIP seen in the perivascular saline represent gross leaks from side branch arteries that were incompletely cauterized. In future *ex vivo* work, porcine arteries, which more closely resemble human tissue, without side branches in the test segment will be employed. Without such alternative flow paths, this model will allow quantification of therapeutic delivery across the arterial wall into the perivascular space.

No tissue damage was observed in this study in arteries with or without ultrasound exposure. Factor VIII staining verified the survival of an intact endothelium throughout handling and ultrasound exposure of the artery. Arteries in which Rh-ELIP were observed to penetrate beyond the endothelium did not exhibit cellular damage, when compared with untreated controls. Several investigators using commercially available echo contrast agents in the peripheral circulation and brain [44], [45] in rabbit models have noted vascular leakage and apoptosis in vascular cells exposed to 1- to 1.5-MHz pulsed ultrasound at peak-to-peak pressure amplitudes between 2 and 36 MPa. Our results in *ex vivo* murine arteries exposed to 1-MHz CW ultrasound at a peak-to-peak pressure amplitude of 0.49 MPa did not exhibit such damage, likely due to the smaller bubbles and lower ultrasound pressure amplitudes employed in this study.

The mechanism of US-induced opening of endothelial tight junctions has not yet been elucidated. However, we postulate the following. An endothelial cell inwardly-rectifying potassium channel complex (Kir6/SUR) has been reported to act as a mechanochemical transducer [46], [47], [48]. Opening of this channel in response to mechanical stimulation (either from the motion of the stably cavitating bubble wall itself or from the microstreaming surrounding the bubble) leads to influx of potassium into the endothelial cell, membrane depolarization leading to opening of voltage-dependent calcium channels, influx of calcium and activation of endothelial nitric oxide synthase [49]. Elevated nitric oxide in endothelial cells has been shown to lead to tight junction opening [49].

Future studies are needed to examine the effects of treatment time on delivery of liposomes to and beyond the endothelium. Additional studies are also needed to optimize the degree of cavitation in order to achieve maximal liposome targeting and penetration while minimizing deleterious bioeffects. A more efficient delivery might also be achieved by varying the scheme

for injecting liposomes, using a sustained injection or a series of injections rather than a single bolus.

Conclusion

This work demonstrates ultrasound-enhanced anti-ICAM-1-targeted Rh-ELIP penetration beyond the murine aorta endothelium as determined using fluorescence histology. The model allowed detection of bubble activity hypothesized to enable passage of molecules through vascular endothelial tight junctions. This *ex vivo* vascular model has the potential to provide a versatile tool to researchers exploring ultrasound-mediated delivery of therapeutics to the arterial wall.

Acknowledgments

The authors' sincere thanks go to Melanie Moody and Shaoling Huang of the University of Texas Health Science Center, Houston, for their assistance with tissue preservation techniques, to Yuejiao Zou for the production of the liposomes, and to Steven Kolodziej and Patricia Navarro for preparing negative staining TEM images of the ELIP and providing guidance in identifying structural features visible in them. The authors would also like to thank Bill Brauntz of the University of Cincinnati for his outstanding work on the artery mounting system. This project was supported by NIH award number NS047603 from the NINDS, NIH award number T32GM063483 from the NIGMS, the Albert J. Ryan Foundation, and the Rindsberg Memorial Fund.

References

1. Groothuis DR. The blood-brain and blood-tumor barriers: A review of strategies for increasing drug delivery. Neurooncology 2000;2(1):45–59.
2. Eccleston DS, Horrigan MC, Ellis SG. Rationale for local drug delivery. Seminars in interventional cardiology : SIIC 1996;1(1):8–16. [PubMed: 9552480]
3. Gregoriadis G. Homing of liposomes to target cells. Biochemical Society Transactions 1975;3(5):613–618. [PubMed: 53164]
4. Drummond DC, Noble CO, Guo Z, Hayes ME, Connolly-Ingram C, Gabriel BS, Hann B, Liu B, Park JW, Hong K, Benz CC, Marks JD, Kirpotin DB. Development of a highly stable and targetable nanoliposomal formulation of topotecan. J. Control. Release 2010;141(1):13–21. [PubMed: 19686789]
5. Klegerman ME, Wassler M, Huang S, Zou Y, Kim H, Shelat HS, Holland CK, Geng Y, McPherson DD. Liposomal modular complexes for simultaneous targeted delivery of bioactive gases and therapeutics. J. Control. Release.
6. Kee PH, Abruzzo TA, Smith DA, Kopechek JA, Wang B, Huang SL, MacDonald RC, Holland CK, McPherson DD. Synthesis, acoustic stability, and pharmacologic activities of papaverine-loaded echogenic liposomes for ultrasound controlled drug delivery. Journal of liposome research 2008;18 (4):263–277. [PubMed: 18720194]
7. Kopechek JA, Abruzzo TM, Wang B, Chrzanowski SM, Smith DA, Kee PH, Huang S, Collier JH, McPherson DD, Holland CK. Ultrasound-mediated release of hydrophilic and lipophilic agents from echogenic liposomes. J Ultrasound Med 2008;27(11):1597–1606. [PubMed: 18946099]
8. Tiukinhoy-Laing SD, Parikh DS, Huang SL, Martinez J, Kane B, MacDonald RC, McPherson DD. Ultrasound-enhanced in vivo delivery of agents into arterial media using echogenic immunoliposomes. Circulation 2005;112:634.
9. Klegerman ME, Huang S, Parikh D, Martinez J, Demos SM, Onyuksel HA, McPherson DD. Lipid contribution to the affinity of antigen association with specific antibodies conjugated to liposomes. Biochimica et Biophysica Acta - Biomembranes 2007;1768(7):1703–1716.
10. Poston RN, Haskard DO, Coucher JR, Gall NP, Johnson-Tidey RR. Expression of intercellular adhesion molecule-1 in atherosclerotic plaques. American Journal of Pathology 1992;140(3):665–673. [PubMed: 1372160]

11. Kitagawa K, Matsumoto M, Sasaki T, Hashimoto H, Kuwabara K, Ohtsuki T, Hori M. Involvement of ICAM-1 in the progression of atherosclerosis in APOE-knockout mice. Atherosclerosis 2002;160 (2):305–310. [PubMed: 11849652]
12. Kornmann LM, Reesink KD, Reneman RS, Hoeks APG. Critical Appraisal of Targeted Ultrasound Contrast Agents for Molecular Imaging in Large Arteries. Ultrasound Med. Biol 2010;36(2):181–191. [PubMed: 20018434]
13. Apfel RE. Acoustic cavitation prediction. J. Acoust. Soc. Am 1981;69(6):1624–1633.
14. Apfel RE. Acoustic cavitation: A possible consequence of biomedical uses of ultrasound. Br. J. Cancer 1982;45:140–146. [PubMed: 7059457]
15. Carstensen EL, Flynn HG. The potential for transient cavitation with microsecond pulses of ultrasound. Ultrasound in Medicine and Biology 1982;8(6):L720–L724. [PubMed: 7164178]
16. Flynn HG. Generation of transient cavities in liquids by microsecond pulses of ultrasound. J. Acoust. Soc. Am 1982;72(6):1926–1932.
17. Flynn HG, Church CC. Mechanism for the generation of cavitation maxima by pulsed ultrasound. J. Acoust. Soc. Am 1984;76(2):505–512. [PubMed: 6481000]
18. Atchley AA, Frizzell LA, Apfel RE, Holland CK, Madanshetty S, Roy RA. Thresholds for cavitation produced in water by pulsed ultrasound. Ultrasonics 1988;26(5):280–285. [PubMed: 3407017]
19. Holland CK, Apfel RE. Thresholds for transient cavitation produced by pulsed ultrasound in a controlled nuclei environment. J. Acoust. Soc. Am 1990;88(5):2059–2069. [PubMed: 2269722]
20. Holland CK, Apfel RE. Improved theory for the prediction of microcavitation thresholds. IEEE Trans. Ultrason. Ferroelectr. Freq. Control 1989;36(2):204–208. [PubMed: 18284969]
21. Holland CK, Roy RA, Apfel RE, Crum LA. In Vitro detection of cavitation induced by a diagnostic ultrasound system. IEEE Trans. Ultrason. Ferroelectr. Freq. Control 1992;39(1):95–101. [PubMed: 18263123]
22. Deng CX, Xu Q, Apfel RE, Holland CK. In vitro measurements of inertial cavitation thresholds in human blood. Ultrasound in Medicine and Biology 1996;22(7):939–948. [PubMed: 8923712]
23. Deng CX, Xu Q, Apfel RE, Holland CK. Inertial cavitation produced by pulsed ultrasound in controlled host media. J. Acoust. Soc. Am 1996;100(2):1199–1208. [PubMed: 8759969]
24. Holland CK, Deng CX, Apfel RE, Alderman JL, Fernandez LA, Taylor KJW. Direct evidence of cavitation in vivo from diagnostic ultrasound. Ultrasound in Medicine and Biology 1996;22(7):917–925. [PubMed: 8923710]
25. Coussios CC, Roy RA. Applications of Acoustics and Cavitation to Noninvasive Therapy and Drug Delivery. Annu. Rev. Fluid Mech 2008;40(1):395–420.
26. Phelps AD, Leighton TG. The Subharmonic Oscillations and Combination-Frequency Subharmonic Emissions from a Resonant Bubble: Their Properties and Generation Mechanisms. Acustica 1997;83 (1):59–66.
27. ANSI. Bubble detection and Cavitation Monitoring. 2002
28. Holland CK, Vaidya SS, Datta S, Coussios C, Shaw GJ. Ultrasound-enhanced tissue plasminogen activator thrombolysis in an in vitro porcine clot model. Thromb. Res 2008;121(5):663–673. [PubMed: 17854867]
29. Datta S, Coussios CC, McAdory LE, Tan J, Porter T, De Courten-Myers G, Holland CK. Correlation of cavitation with ultrasound enhancement of thrombolysis. Ultrasound in Medicine and Biology 2006;32(8):1257–1267. [PubMed: 16875959]
30. Huang S, McPherson DD, MacDonald RC. A novel pressure/freeze method to form gas and drug co-encapsulated liposomes. Am Assoc Pharm Soc 2006a:W5173.
31. Huang SL, Hamilton AJ, Nagaraj A, Tiukinhoy SD, Klegerman ME, McPherson DD, Macdonald RC. Improving ultrasound reflectivity and stability of echogenic liposomal dispersions for use as targeted ultrasound contrast agents. J. Pharm. Sci 2001;90(12):1917–1926. [PubMed: 11745750]
32. Pozharski EV, McWilliams L, MacDonald RC. Relationship between turbidity of lipid vesicle suspensions and particle size. Anal. Biochem 2001;291(1):158–162. [PubMed: 11262170]
33. Lasch, J.; Weissig, V.; Brandl, M. Preparation of liposomes. In: Torchilin, VP.; Weissig, V., editors. Liposomes. New York: Oxford University Press; 2003. p. 24-25.

34. Kopechek JA, Porter TM, Coussios C, Perrin SR, Huang S, McPherson DD, Holland CK. Acoustic characterization of echogenic liposomes: attenuation and quantitative backscatter. J Acoust Soc Am 2009;125(4)
35. Huo Y, Guo X, Kassab GS. The flow field along the entire length of mouse aorta and primary branches. Ann. Biomed. Eng 2008;36(5):685–699. [PubMed: 18299987]
36. Demos SM, Alkan-Onyuksel H, Kane BJ, Ramani K, Nagaraj A, Greene R, Klegerman M, McPherson DD. In vivo targeting of acoustically reflective liposomes for intravascular and transvascular ultrasonic enhancement. Journal of the American College of Cardiology 1999;33(3):867–875. [PubMed: 10080492]
37. Hamilton AJ, Huang SL, Warnick D, Rabbat M, Kane B, Nagaraj A, Klegerman M, McPherson DD. Intravascular Ultrasound Molecular Imaging of Atheroma Components In Vivo. J. Am. Coll. Cardiol 2004;43(3):453–460. [PubMed: 15013130]
38. Datta S, Coussios C, Ammi AY, Mast TD, de Courten-Myers GM, Holland CK. Ultrasound-enhanced thrombolysis using Definity® as a cavitation nucleation agent. Ultrasound Med. Biol. 2008 In Press.
39. Geng YJ, Klegerman ME, Holland CK, McPherson DD. Targeted delivery of stem cells to atherosclerotic arteries using immunoliposomes. Atherosclerosis Supplements 2009;10
40. Herbst SM, Klegerman ME, Kim H, Shelat H, Wassler M, Moody MR, Yang C-M, Ge X, Zou Y, Kopechek JA, Clubb FJ, Kraemer DC, Huang S, Holland CK, McPherson DD, Geng YJ. Delivery of Stem Cells to Porcine Arterial Wall with Echogenic Liposomes Conjugated to Antibodies against CD34 and Intercellular Adhesion Molecule-1. Molecular Pharmaceutics. 2009 In Press.
41. Kodama T, Tomita N, Horie S, Sax N, Iwasaki H, Sazuki R, Maruyama K, Mori S, Manabu F. Morphological study of acoustic liposomes using transmission electron microscopy. Journal of Electron Microscopy Advance Access. 2009 (November 11, 2009.).
42. Bloemen PGM. Adhesion molecules: A new target for immunoliposome-mediated drug delivery. FEBS Letters 1995;357(2):140–144. [PubMed: 7805880]
43. Mastrobattista E, Storm G, Van Bloois L, Reszka R, Bloemen PGM, Crommelin DJA, Henricks PAJ. Cellular uptake of liposomes targeted to intercellular adhesion molecule-1 (ICAM-1) on bronchial epithelial cells. Biochimica et Biophysica Acta - Biomembranes 1999;1419(2):353–363.
44. Hwang JH, Brayman AA, Reidy MA, Matula TJ, Kimmey MB, Crum LA. Vascular effects induced by combined 1-MHz ultrasound and microbubble contrast agent treatments in vivo. Ultrasound in Medicine and Biology 2005;31(4):553–564. [PubMed: 15831334]
45. Hynynen K, McDannold N, Martin H, Jolesz FA, Vykhodtseva N. The threshold for brain damage in rabbits induced by bursts of ultrasound in the presence of an ultrasound contrast agent (Optison). Ultrasound Med. Biol 2003;29(3):473–481. [PubMed: 12706199]
46. Karpowich N, Martsinkevich O, Millen L, Yuan Y, Dai PL, MacVey K, Thomas PJ, Hunt JF. Crystal structures of the MJ1267 ATP binding cassette reveal an induced-fit effect at the ATPase active site of an ABC transporter. Structure 2001;9(7):571–586. [PubMed: 11470432]
47. Zingman LV, Hodgson DM, Bienengraeber M, Karger AB, Kathmann EC, Alekseev AE, Terzic A. Tandem function of nucleotide binding domains confers competence to sulfonylurea receptor in gating ATP-sensitive K+ channels. J. Biol. Chem 2002;277(16):14206–14210. [PubMed: 11825892]
48. Jöns T, Wittschieber D, Beyer A, Meier C, Brune A, Thomzig A, Ahnert-Hilger G, Veh RW. K+-ATP-channel-related protein complexes: Potential transducers in the regulation of epithelial tight junction permeability. J. Cell. Sci 2006;119(15):3087–3097. [PubMed: 16820413]
49. Handa O, Stephen J, Cepinskas G. Role of endothelial nitric oxide synthase-derived nitric oxide in activation and dysfunction of cerebrovascular endothelial cells during early onsets of sepsis. American Journal of Physiology - Heart and Circulatory Physiology 2008;295(4):H1712–H1719. [PubMed: 18723768]

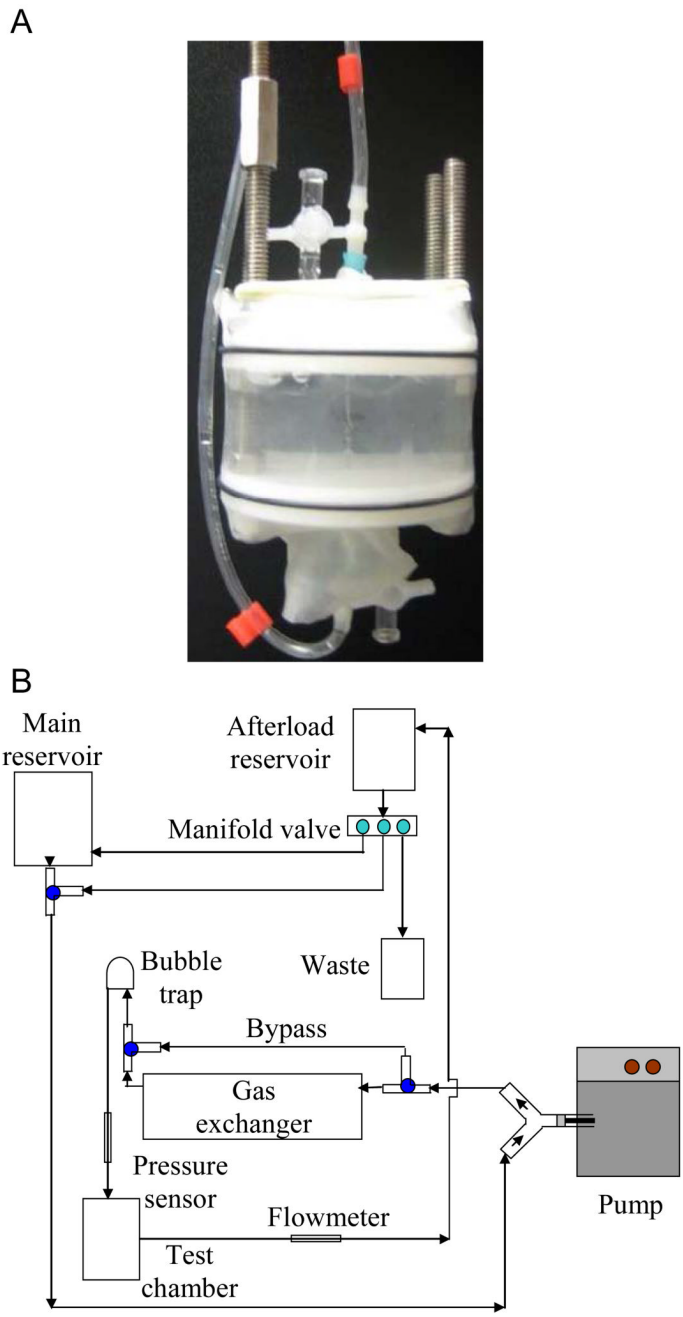

Figure 1.
Panel A illustrates an artery mounted in the sample holder with perivascular saline. Panel B shows a schematic of the artery flow system. The perfusate (0.5% bovine serum albumin in phosphate buffered saline) is maintained at 95% oxygenation and 37° C by way of a gas exchanger and extensive circulated water jacketing.

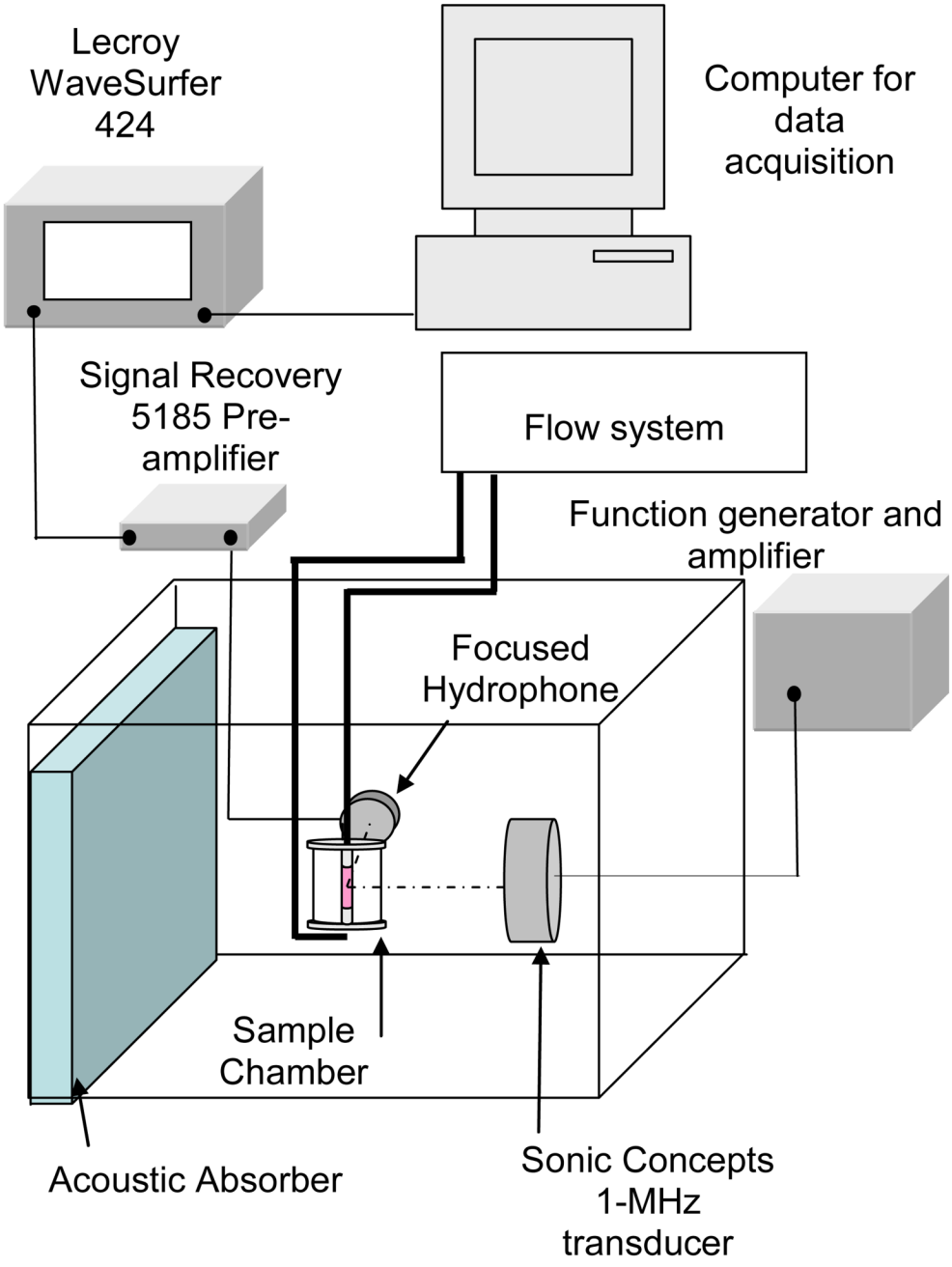

Figure 2.
Apparatus for insonification of mouse aorta and cavitation detection.

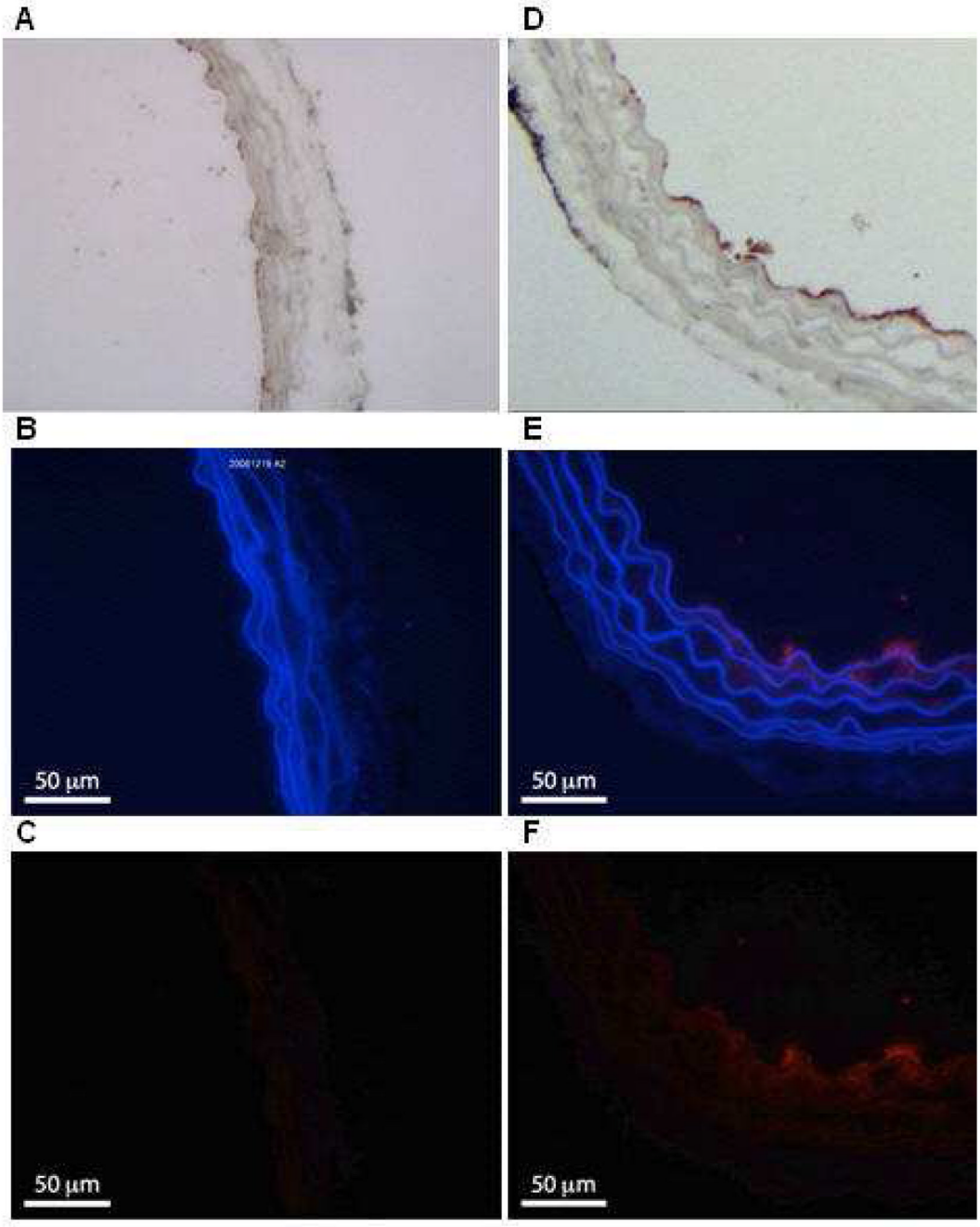

Figure 3.
Examples of our fluorescent Rh-ELIP data. Panels A – C show an artery treated with Rh-ELIP alone, while D – F show an artery treated with a combination of Rh-ELIP and CW ultrasound (0.49 MPa peak-to-peak amplitude). A and D show arteries stained with Factor VIII to highlight the endothelium. B and E show the arterial walls as viewed with a blue filter, superimposed over the same segment viewed with a red filter. C and F show the red-filtered image alone, where the increased fluorescence in Panel F is due to the presence of Rhodamine. The full scale bar is 100 μm.

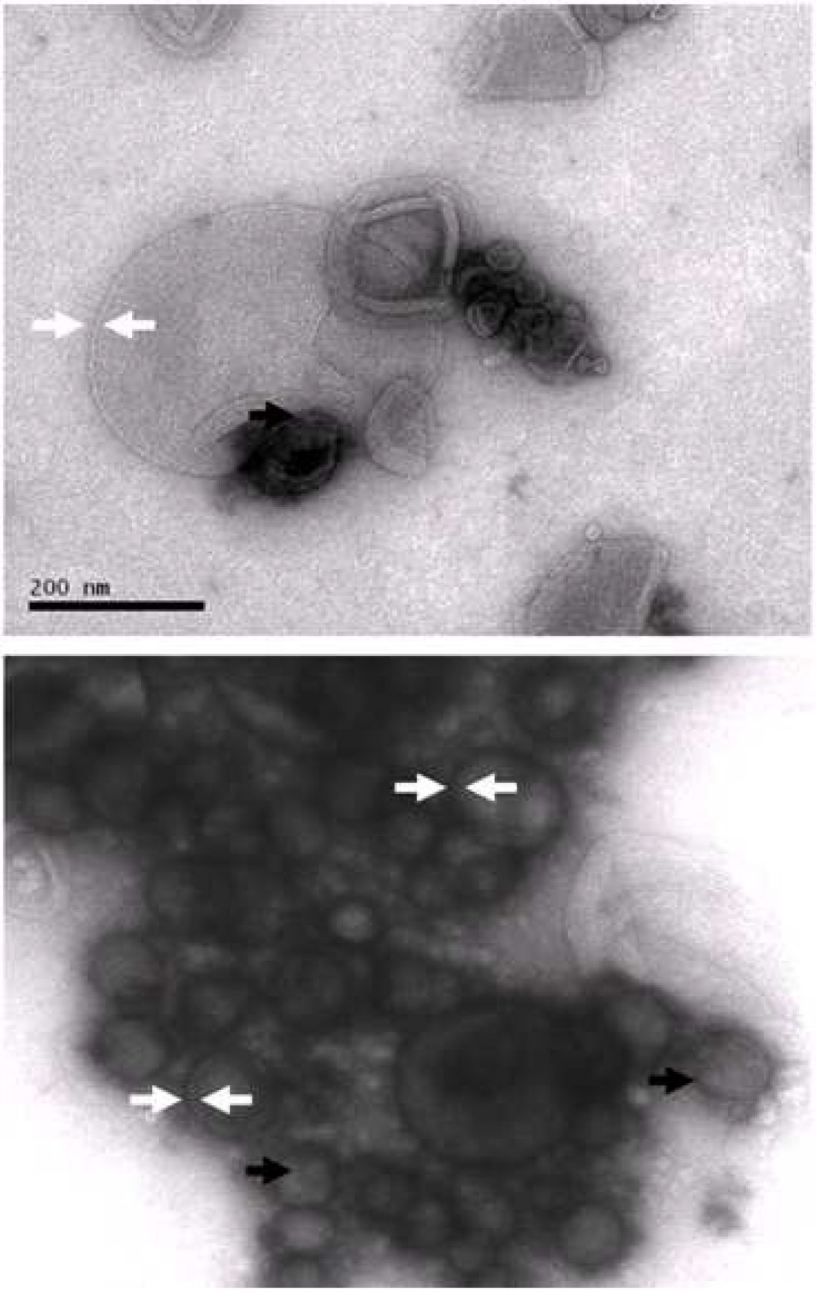

Figure 4.
In these 150,000X images, lipid bilayers (white arrows, tips 11 nm apart) are visible in several echogenic liposomes. Black arrows indicate visible gas bubbles apparently surrounded by a phospholipid monolayer within liquid-filled liposomes.

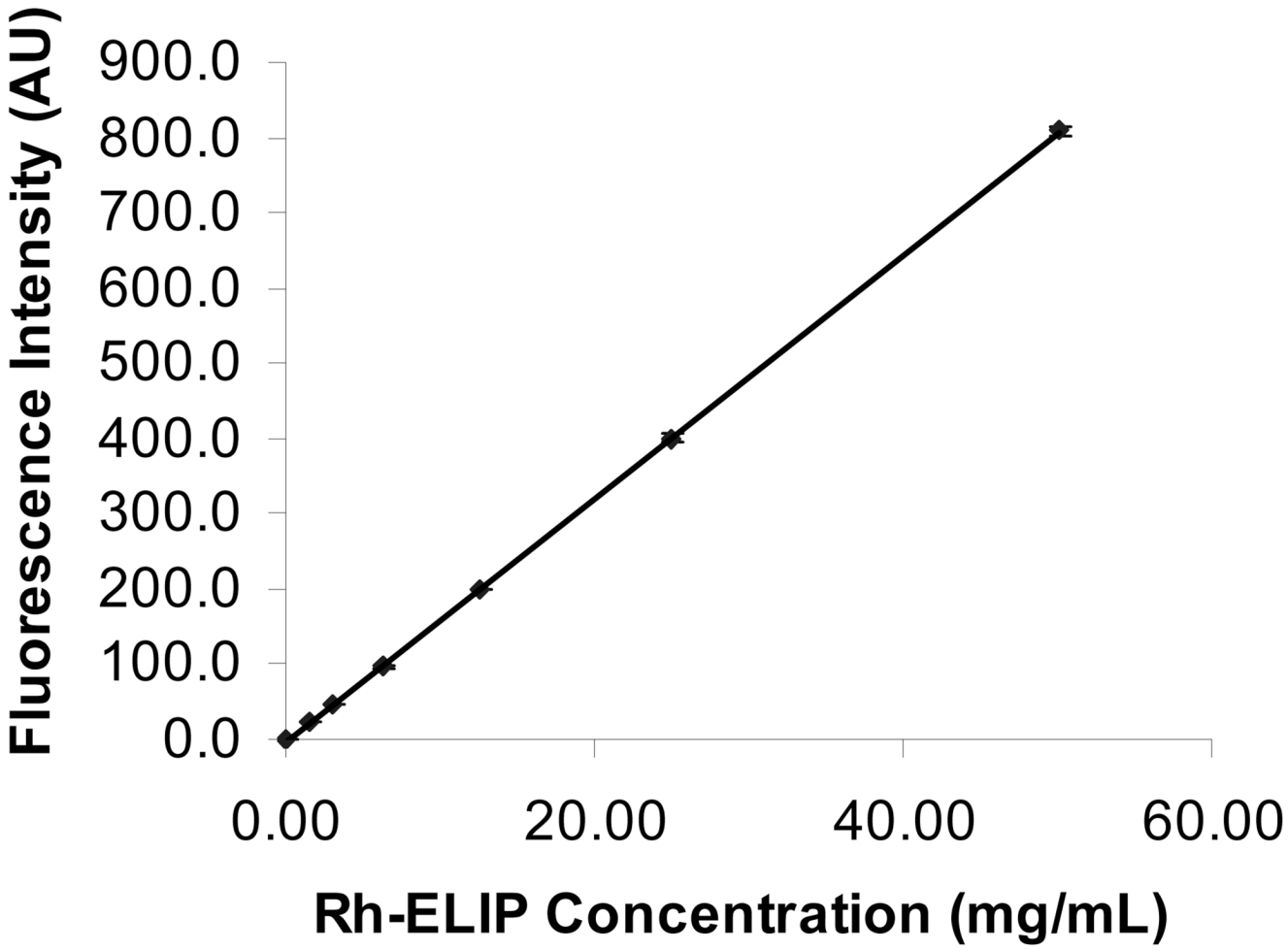

Figure 5.
The fluorescence emission intensity of Rh-ELIP in arbitrary units (A.U) as a function of lipid concentration in normal saline. Solutions of Rh-ELIP were excited at 567 nm and fluorescence emission intensity was quantified at 589 nm. The line overlapping the data points is a linear fit of the form $y(x) = mx + b$. Average ± one standard deviation, n = 3 samples per data set.

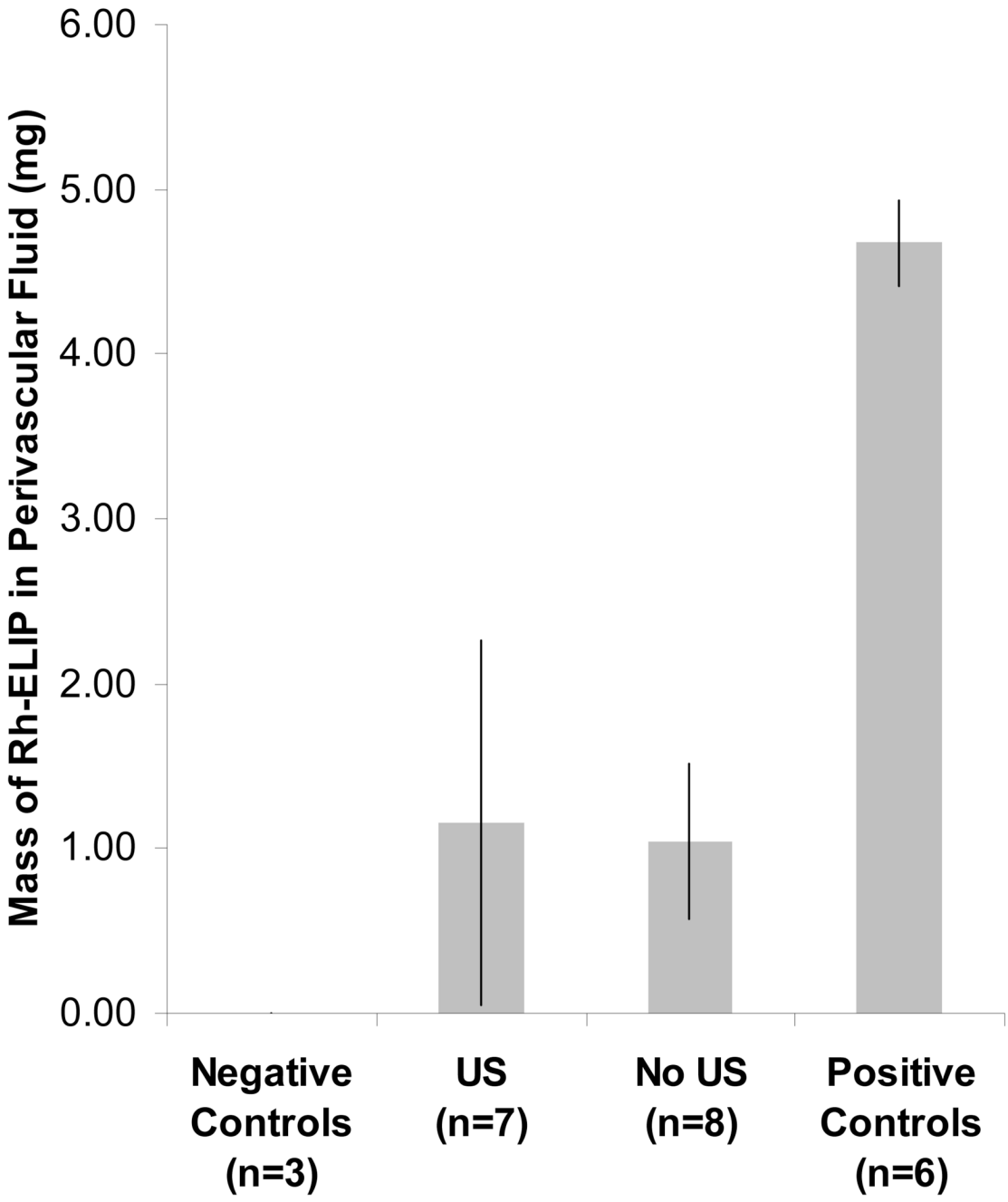

Figure 6.
Mass of Rh-ELIP in saline surrounding *ex vivo* mouse aorta following intraluminal bolus of Rh-ELIP in flow of BSA. Error bars indicate one standard deviation. Results are of three controls, seven ultrasound treated arteries, eight arteries with no ultrasound, and six positive controls (bolus of Rh-ELIP delivered directly into perivascular saline).

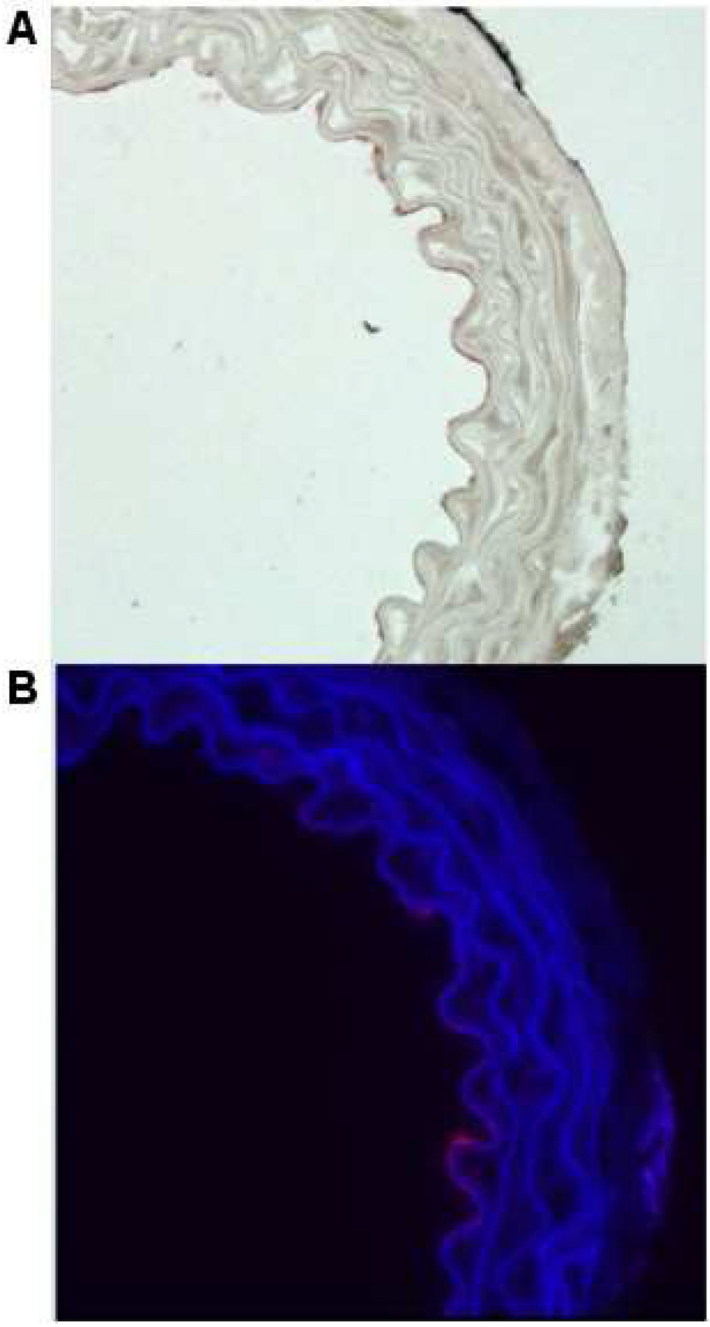

Figure 7.
Co-location of Rh-ELIP with ICAM-1 expression was verified by staining with rat antibody against mouse ICAM-1 (brown stain on luminal surface in A), and observing adjacent slices for Rhodomine fluorescence (B).

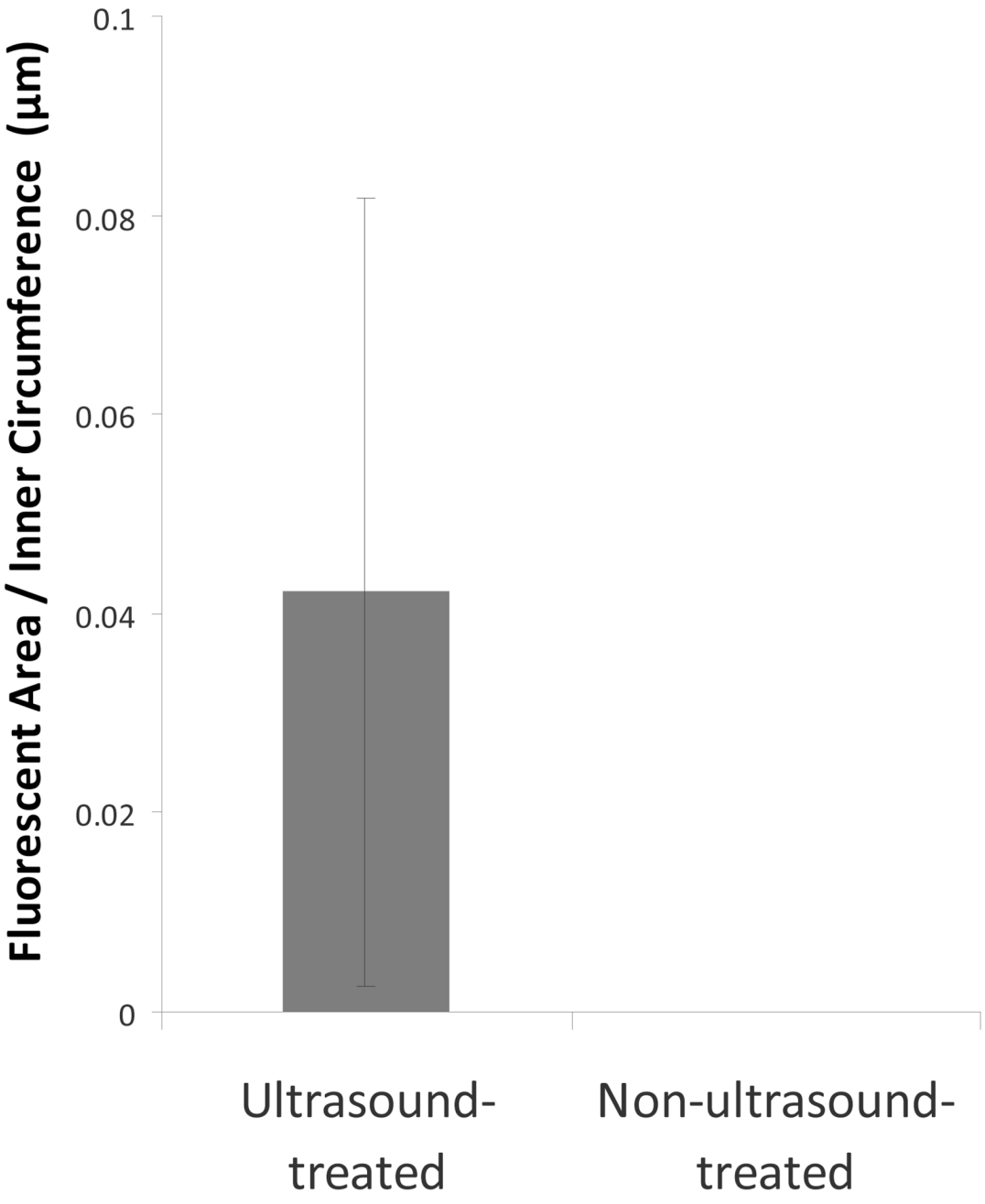

Figure 8.
Penetration of fluorescent Rh-ELIP beyond the arterial endothelium, normalized by perimeter of the arterial lumen. This was calculated from histological images by summing the red pixels (with each weighted by its intensity), and using a scale in the image to convert from pixel area to μm^2. This red area was then divided by the inner perimeter of the artery to account for variations in artery size.